

Article

Electrochemical Characteristics of Nanosized Cu, Ni, and Zn Cobaltite Spinel Materials

Mohamed Mokhtar M. Mostafa ^{1,*}, Wejdan Bajafar ¹, Lin Gu ², Katabathini Narasimharao ¹, Mohamed Abdel Salam ¹, Abdulmohsen Alshehri ¹, Nezar H. Khdayr ³, Sulaiman Al-Faifi ¹ and Abhishek Dutta Chowdhury ^{2,*}

¹ Chemistry Department, Faculty of Science, King Abdulaziz University, Jeddah 21589, Saudi Arabia

² College of Chemistry and Molecular Sciences, Wuhan University, Wuhan 430072, China

³ King Abdulaziz City for Science and Technology, Riyadh 11442, Saudi Arabia

* Correspondence: mmoustafa@kau.edu.sa (M.M.M.M.); abhishek@whu.edu.cn (A.D.C.)

Abstract: For a long time, transition metal oxide systems have been considered well explored materials in heterogeneous catalysis. Amongst, the spinel-type oxides, materials such as cobaltites (Co_3O_4) received significant attention, owing to their use in many industrial applications. In the present study, nanosized Cu, Ni, and Zn cobaltite spinel oxides were synthesized by a simple hydrothermal method. Physicochemical characterization of the synthesized materials was performed utilizing XRD, HRTEM, CO_2 -TPD, and XPS techniques. The textural characteristics (BET-surface area, pore size, etc.) of samples were determined from N_2 physisorption measurements at -196°C . The CO_2 -electrocatalytic reduction was selected as a model reaction to evaluate the electrochemical performance of the synthesized spinel cobaltites. For Ni, Cu, and Zn spinel materials, hydrogen was produced as the main product at the whole potential, along with other products, such as CO and HCOOH. Despite the advantages, the catalytic electrochemical CO_2 reduction performance of spinel cobaltite catalysts is still far from adequate, which is principally ascribed to the low number of active sites combined with poor electrical conductivity.

Keywords: nanosized; spinel cobaltites; electrochemical properties; electrocatalysis; CO_2 -electrocatalytic reduction



Citation: Mostafa, M.M.M.; Bajafar, W.; Gu, L.; Narasimharao, K.; Abdel Salam, M.; Alshehri, A.; Khdayr, N.H.; Al-Faifi, S.; Chowdhury, A.D. Electrochemical Characteristics of Nanosized Cu, Ni, and Zn Cobaltite Spinel Materials. *Catalysts* **2022**, *12*, 893. <https://doi.org/10.3390/catal12080893>

Academic Editors: Ali Seifitokaldani and Carlo Santoro

Received: 17 June 2022

Accepted: 11 August 2022

Published: 13 August 2022

Publisher's Note: MDPI stays neutral with regard to jurisdictional claims in published maps and institutional affiliations.



Copyright: © 2022 by the authors. Licensee MDPI, Basel, Switzerland. This article is an open access article distributed under the terms and conditions of the Creative Commons Attribution (CC BY) license (<https://creativecommons.org/licenses/by/4.0/>).

1. Introduction

In the past decades, researchers utilized noble metal (Au, Ag, and Pd) based electrocatalysts to obtain superior performances for electrochemical reduction of CO_2 [1]. However, these catalysts are less selective, expensive, have limited availability, and their catalytic properties decline rapidly. Therefore, it is necessary to find an inexpensive alternative catalyst to obtain enhanced catalytic performance in CO_2 electrochemical reduction [1,2]. Recently, transition metal oxide-based electrocatalysts have provoked increasing attention [2]. These materials possessed additional advantages, such as high abundance, low cost, and easy preparation [3]. The widest class of materials examined in electrocatalysis is the transition metal oxide systems, which have been employed for a long time in heterogeneous catalysis. The research was focused on dioxides, perovskites, pyrochlores, and spinel-type transition metal oxides [4]. Among them, spinel type oxides have received great interest due to their unique crystal structure and chemical and thermal stability. Spinel type oxides typically expressed with the general formula of AB_2O_4 , where A^{II} is a divalent cation, e.g., Mn, Co, Mg, Fe, Cr, Zn, Ni, and Cu, and B^{III} is a trivalent cation, e.g., Al, Ti, Ga, V, Cr, Mn, Fe, Co, and Ni [5,6]. Many of spinel oxides have intriguing electronic, optical, and magnetic properties, making them suitable for a wide range of technological applications [5].

Numerous metal oxides have been studied extensively as electrocatalysts, including Co_3O_4 -based catalysts [7–10] for oxidation of water, oxygen reduction reactions, and

hydrogen evolution processes. Nanostructured spinel Co_3O_4 's electrochemical activity is mainly due to the presence of mixed oxidation states (Co^{2+} in tetrahedral and Co^{3+} in octahedral sites) and highly active surface sites [11]. According to Gao et al., ultrathin layers of Co_3O_4 exhibit strong CO_2 reduction activity and are particularly selective for a formic acid generation [12]. Because of the irregular electrical structure of ultrathin films and the ease with which electronic transfer, carrier transport, and low corrosion rate are facilitated by the films, this activity was linked not only to an increased number of surface sites typical of low-dimensional systems. For effective CO_2 adsorption and enhanced H^+ transfer, nanosized Co-based spinel oxides have been shown to have significant CO_2RR activity [5,12] due to the presence of both metal (for an electron transfer into CO_2) and crystalline metal oxide phases. Bulk and transition metal containing cobaltites (Co_3O_4 , NiCo_2O_4 , CuCo_2O_4 and ZnCo_2O_4) are among the spinel-type oxides that have attracted a great deal of attention over the past several decades due to their wide range of industrial applications. Anode and cathode compounds for oxygen evolution reactions have been extensively studied due to their promising activity and stability in alkaline media. These oxide materials are not stable in acidic environments. The benefits of using these oxides as electrode materials include their activity, availability, low cost, thermodynamic stability, low electrical resistance, and friendliness to the environment. There are two types of cubic oxide lattices: normal Co_3O_4 and $\text{M}^{\text{II}}\text{Co}_2\text{O}_4$ (inverted spinel). For decades, Co_3O_4 and NiCo_2O_4 have been known to be active and stable catalysts, not only for oxygen evolution and reduction but also for organic electro-oxidation in alkaline environments [13–18].

There are different methods that can be utilized to prepare spinels, including solid-state, hydrothermal, sol-gel, co-precipitation, solvothermal, and sonochemical techniques [19]. Table S1 summarizes some spinels utilized for the CO_2 reduction reaction, where cobalt containing spinel catalysts resulted in the formation of formic acid. In this context, the present study evaluates the electrochemical characteristics and catalytic activity of metal (Zn, Ni and Cu) spinel cobaltites catalysts for CO_2 reduction.

2. Results and Discussion

The XRD analysis was used to investigate the crystal structure and phase detection of synthesized spinels, and the obtained patterns are shown in Figure 1. Reflections at 19° , 31.6° , 37.4° , and 44.6° correspond to the (110), (220), (310), (400), (511), and (440) planes for the cubic structure of the spinel [20]. The major reflections in the XRD patterns of the spinels can be indexed to NiCo_2O_4 (JCPDS file no. 73-1702), CuCo_2O_4 (JCPDS file no. 1-1155) and ZnCo_2O_4 (JCPDS file no. 23-1390) [21–23]. There were no reflections observed for any other crystal phase, indicating the purity of the synthesized materials. It is interesting to note that the NiCo_2O_4 sample exhibited relatively broad reflections compared to other two samples, indicating the relatively small crystallite size in the case of the NiCo_2O_4 sample. The average crystallite size of the synthesized spinels was calculated by using the Scherrer equation. The calculated average crystallite sizes were 14 nm, 30 nm, and 31 nm for NiCo_2O_4 , ZnCo_2O_4 , and CuCo_2O_4 samples respectively.

The TEM images (Figure 2) show that Ni spinel has a typical three-dimensional porous architecture with interconnected nanowires. High-resolution (HR) TEM images (Figure 2a,b) show that Ni spinel sample contained uniform nanowires with an average diameter of approximately 12 nm. From Figure 2c–f, it can be observed that the Cu spinel and the Zn spinel consist of nonuniform nanoparticles with an average diameter of approximately 30 nm, which is in concurrence with the XRD results.

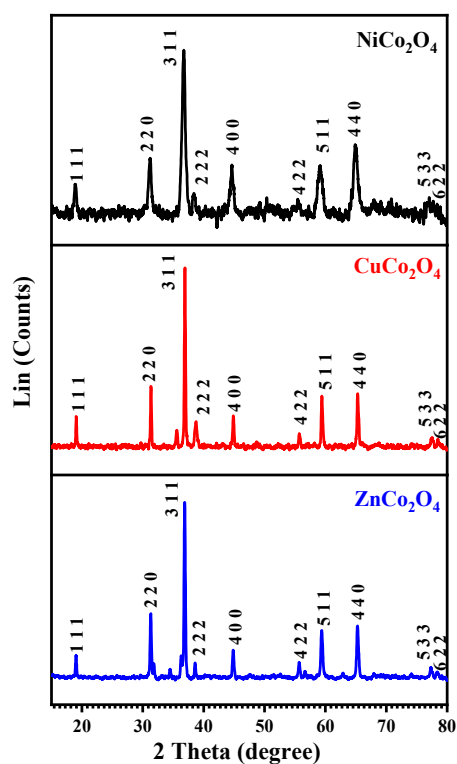


Figure 1. XRD patterns of synthesized NiCo_2O_4 , CuCo_2O_4 , and ZnCo_2O_4 .

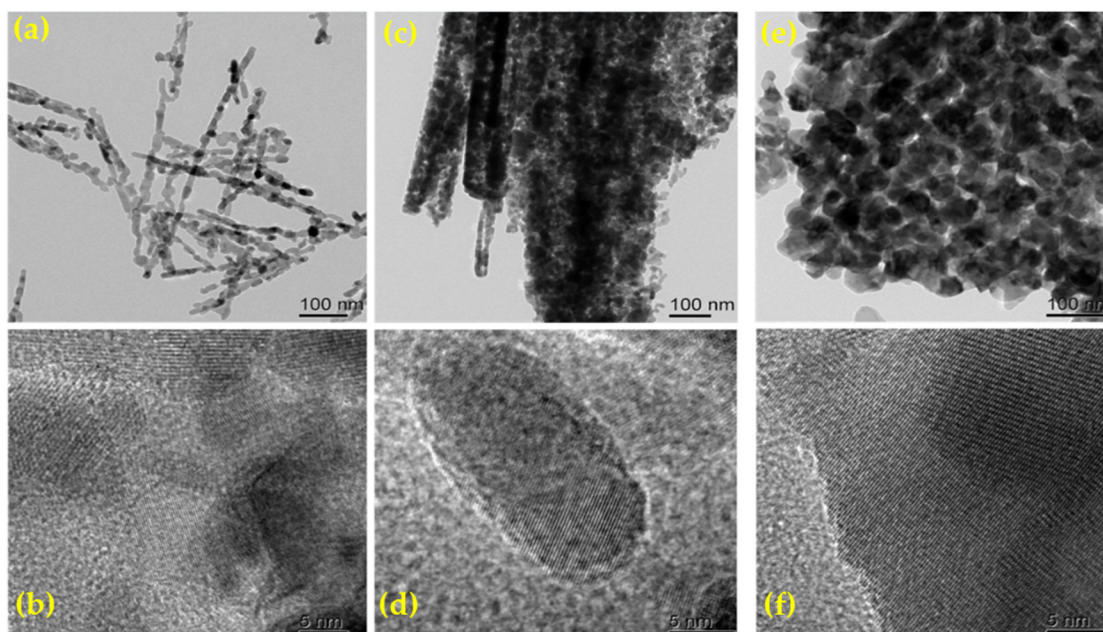


Figure 2. HRTEM images with different magnification for NiCo_2O_4 (a,b), CuCo_2O_4 (c,d), ZnCo_2O_4 (e,f).

Figure 3 illustrates the nitrogen adsorption-desorption isotherms of synthesized spinel catalysts. All the isotherms can be classified as type IV according to IUPAC classification [24,25]. The hysteresis loops in the isotherms indicate the mesoporous nature of all spinels, especially the NiCo_2O_4 . The H3-type hysteresis loop of spinel catalysts indicates that the type of holes is slit pores formed by the aggregation of sheet particles [23,26]. Table 1 displays the BET surface area (S_{BET}), micropore surface area (S_{micro}), mesopore surface area (S_{meso}), total pore volume (V_{total}), micropore volume (V_{micro}), and meso-

pore volume (V_{meso}) of all the investigated samples. The synthesized nanosized NiCo_2O_4 , ZnCo_2O_4 and CuCo_2O_4 spinel catalysts possessed a BET surface area of 41, 32, and $28 \text{ m}^2/\text{g}$, respectively [22,23]. The pore size distribution patterns were obtained by applying the Non-Local Density Functional Theory (NLDFT) method. The obtained patterns indicated that the synthesized samples have multimodal distribution curves in the microporous, mesoporous, and macroporous ranges [21]. S_{meso} and V_{meso} are higher in NiCo_2O_4 spinel than other spinels, indicating that this particular spinel exhibited a larger surface area and mesoporous feature. The hierarchy factor (HF) increases in CuCo_2O_4 and ZnCo_2O_4 spinels, which indicates that the BET surface area was significantly reduced as a function of the pronounced suppression of the mesopore volume of these samples. NLDFT calculations show a high number of pores with a diameter of approximately 2 nm, which is on the edge between micro and mesopores. However, the samples possessed specific surface areas of 41, 28, and $32 \text{ m}^2/\text{g}$, which would be characteristic for materials with much wider pores. The average pore size was calculated as 3 nm, 3 nm, and 13 nm for Cu, Zn, and Ni cobaltite samples, respectively. The presence of a H3 hysteresis loop indicates that the samples have slit-type pores due to the aggregation of spinel particles [23,26]. Therefore, the meso and macro porosity observed in the samples is due to the arrangement of particles, which explains the low surface area of the samples. In general, the presence of micropores is responsible for a high surface area. These observed results indicate that the synthesized spinel materials possessed a relatively high surface area and porosity, which enhance the diffusion of molecules. In addition, the nanowire or nanoparticle morphology could increase the contact area for reacting molecules, providing enough active sites for reactions.

The surface structure and oxidation state of the metals presented in the synthesized spinels were analyzed using XPS analysis. The full survey and deconvoluted XPS spectra for the three samples are shown in Figures S1 and S2, respectively. For the sake of clarity, only $2p_{3/2}$ components for the metal (Cu, Ni, Zn, and Co) species are presented in the figure. The Gaussian fitted XPS spectrum of the CuCo_2O_4 sample shows the presence of Cu, Co, and O elements. It is known that chemical state differentiation is not straight forward with XPS, as the $\text{Cu}2p_{3/2}$ peak for Cu^0 , Cu^+ , and Cu^{2+} species appears in the range of 933–933.5 eV [24,27]. However, it is possible to distinguish the Cu oxidation states; using the satellite peak features of $\text{Cu}2p$ as the Cu (II) species exhibits strong observable satellite features around 943 eV [28]. The presence of strong satellite peaks confirm the characteristic of Cu^{2+} species in the synthesized CuCo_2O_4 sample; therefore, the $\text{Cu} 2p_{3/2}$ peaks observed at 932.9 eV and 934.7 eV could be attributed to Cu (II) oxide and Cu (II) hydroxide species. The $\text{Co}2p$ region present in the synthesized three spinel samples (CuCo_2O_4 , NiCo_2O_4 , and ZnCo_2O_4) and the $\text{Co} 2p_{3/2}$ can be fitted into two peaks. The fitted peaks at 780.0 and 781.6 eV correspond to Co^{3+} and Co^{2+} species. It was reported that bulk cobalt oxide, such as Co_3O_4 , possesses mixed oxidation state of Co^{2+} and Co^{3+} , and it is expected to show satellite features due to both Co^{2+} and Co^{3+} states. Co^{2+} has an observable satellite feature around 786 eV [29]. Moreover, the integral area of the Co^{3+} peak is much larger than that of the Co^{2+} peak, which reveals that the main oxidation state of Co element in the three spinel samples is Co^{3+} [24,27]. The presence of mixed oxidation states of the same cation in spinel systems (Co^{2+} and Co^{3+}) and the presence of highly active surface sites are the primary sources of electrochemical activity in cobaltite spinels. In this case, the ultrahigh part of low-coordinated surface Co atoms may act as the potential active sites for efficiently adsorbing CO_2 [30,31].

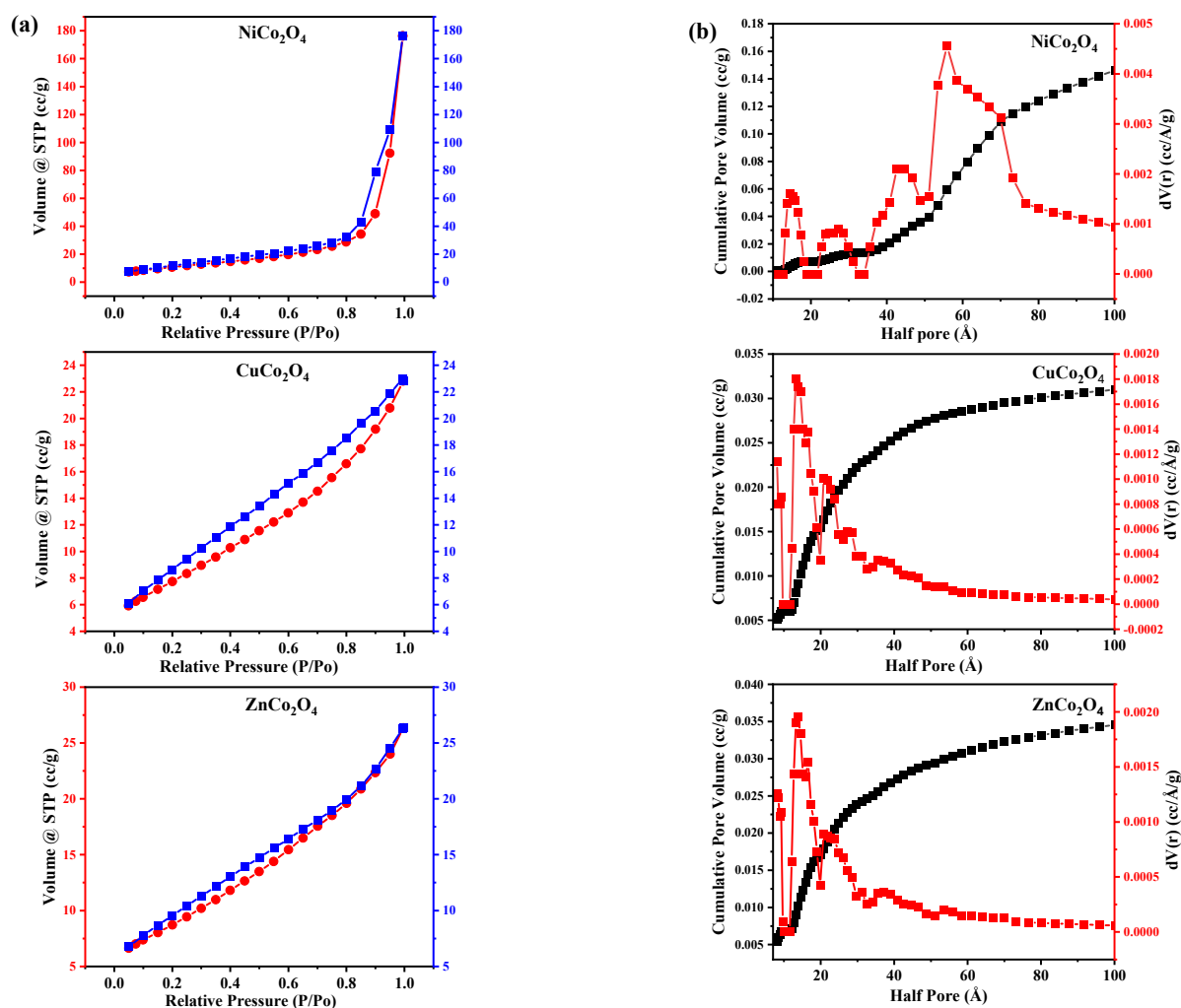


Figure 3. (a) N₂ adsorption-desorption isotherms for NiCo₂O₄, CuCo₂O₄, and ZnCo₂O₄. (b) Pore size distribution curves for NiCo₂O₄, CuCo₂O₄, and ZnCo₂O₄.

Table 1. Textural properties of different spinels from N₂- physisorption at −196 °C.

Sample	S _{BET} (m ² /g)	S _{micro} (m ² /g)	S _{meso} (m ² /g)	V _{total} (cc/g)	V _{micro} (cc/g)	V _{meso} (cc/g)	Average Pore Size (nm)	Pore Radius (nm)	C-Constant	HF
NiCo ₂ O ₄	41	0	35	0.2726	0.000	0.26	13	8.7	45.7	0.000
CuCo ₂ O ₄	28	11	12	0.0352	0.007	0.023	3	1.7	121.6	0.088
ZnCo ₂ O ₄	32	12	16	0.0407	0.007	0.027	3	1.7	100.5	0.086

It is well reported that Ni contained spinels can show complex multiplet-split peaks [32]. The Ni 2p_{3/2} can be fitted into two peaks at 855.7 eV and 858.3 eV. The first peak could be assigned to Ni³⁺ and the other peak at 858.3 eV could be related to Ni²⁺ cations in octahedral or tetrahedral sites of the NiCo₂O₄ spinel structure. This binding energy could be assigned to Ni cations or surface Ni(OH)₂ species [33]. The Zn 2p_{3/2} component showed a strong peak at 1021.0 eV, corresponding to the Zn²⁺ in the ZnCo₂O₄ structure. It was also observed that the binding energy different between the Zn 2p_{3/2} and Zn 2p_{1/2} peaks is approximately 23 eV, which is in accordance with Hu et al. [34].

The O 1s spectra of three samples can be fitted into three peaks. The peak at 529.5 eV matches to the oxygen in the crystal lattice that bonded with metal ions, the peak at 531.5 eV corresponds to the oxygen of OH[−] groups, and the peak at 533.3 eV corresponds to the oxygen of physically adsorbed H₂O molecules [20,24]. These observations clearly

indicating that the surfaces of synthesized spinels are hydroxylated, which could be useful functional groups for catalyzing different types of reactions.

CO₂-TPD experiments were performed to evaluate the number of active sites presented in the synthesized spinel catalysts to adsorb the CO₂ molecules. The CO₂-TPD patterns obtained for the three samples are shown in Figure 4. The deconvolution of the desorption peaks for TPD pattern of the NiCo₂O₄ sample indicates the presence of two desorption peaks in the temperature range of 430–730 °C, while the CuCo₂O₄ sample exhibited between 500 and 770 °C. However, the ZnCo₂O₄ sample yielded peaks between 625 and 730 °C. In addition, the samples showed intense and broad CO₂ desorption peaks at high temperatures, and these observed results indicated that the samples possessed strong CO₂ adsorption ability. Furthermore, it was found that the NiCo₂O₄ catalyst can adsorb a large number of CO₂ molecules (1089.1 μmol/g compared to the other two samples (Table 2)). Similar results were previously observed that NiCo₂O₄ catalyst has a higher CO₂ adsorption ability than both copper and zinc cobaltites [35].

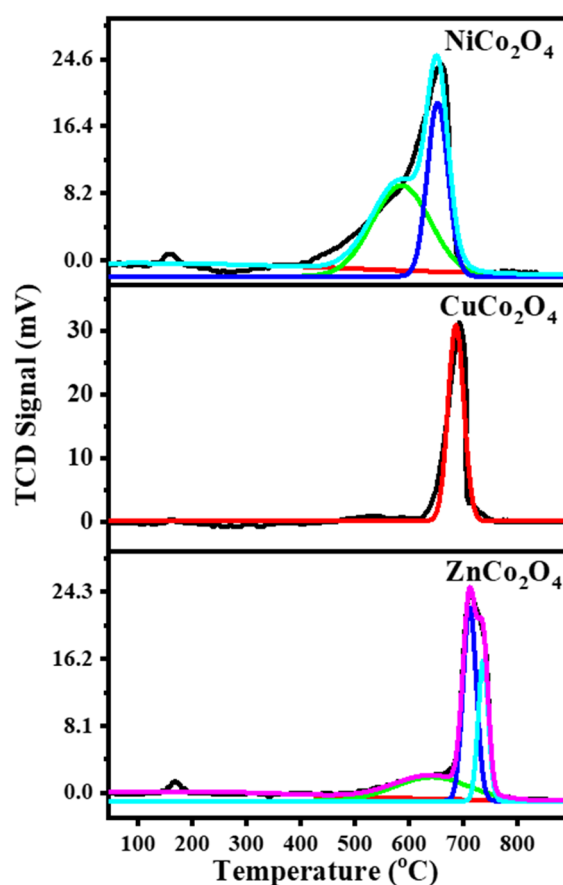


Figure 4. CO₂-TPD patterns for NiCo₂O₄, CuCo₂O₄ and ZnCo₂O₄ samples.

Table 2. Data obtained from CO₂-TPD measurements for the investigated samples.

Catalyst	Temp. (°C)	CO ₂ Uptake (μmol/g)	Total CO ₂ Uptake (μmol/g)
NiCo ₂ O ₄	585.5	646.6	1089.1
	652	442.5	
CuCo ₂ O ₄	686.2	626.2	626.4
ZnCo ₂ O ₄	620.8	152	697.7
	720	545.8	

3. Catalytic Activity

Using an H-cell separated by a Nafion proton exchange membrane, the catalytic activity of Ni spinel, Cu spinel, and Zn spinel for CO₂ reduction was measured. There was a sealed compartment for the working electrode and the reference electrode (Ag/AgCl electrode) and a separate compartment for the counter electrode (Pt electrode). Three electrodes were used to measure the linear sweep voltammetry (LSV) of the catalysts in CO₂ saturated 0.1 M KHCO₃ aqueous solution. As a result, the current density was normalized to the area of the carbon paper electrode, approximately 1 cm². Figure 5a shows the LSV scans of the spinel catalysts. In terms of potential range, the current density of Ni spinel is much higher than that of Cu and Zn spinel. It suggests that Cu and Zn spinel has a lower overpotential to reduce CO₂ than other spinel materials. As shown in Figures S3–S5, the Ni, Zn, and Cu materials were also evaluated at different times in CO₂-saturated 0.1 M KHCO₃ and reproduced independently by two separate systems. This observation supports its practical applicability in terms of efficiency, flexibility, and durability. To further gain insights into the intrinsic activity of the Ni, Cu, and Zn spinel, measurement of double layer capacitance (C_{dl}) was herein tested, which is proportional to the electrocatalytic active surface areas (ECSA) in the electrocatalysts [36] (Figures S6–S8). As shown in Figure 5b, the C_{dl} of Cu spinel is \approx 1.85 and 1.12 times higher than that of Zn and Ni spinel, suggesting that the Cu spinel has relatively more exposed active electrocatalytic sites. When the LSV curves are normalized by the ECSA to highlight the intrinsic activity, as shown in Figure 5c, Zn spinel showed relatively better CO₂RR activity than Ni and Cu spinel. Figure S9 shows the Nyquist plots of Ni, Cu, and Zn spinel for CO₂RR, the contact and solution resistance (14.07 Ω) of the Zn spinel is also the lowest among Ni spinel (15.53 Ω) and Cu spinel (16.34 Ω).

To analyze the reduction product of CO₂ and gain insight into the selectivity of the spinel catalysts, steady-state electrolysis was conducted at different potentials from -0.9 to -1.1 V vs. RHE. At each potential, CO₂ reduction reaction was conducted to reach a total electric charge of 50 C. For Ni, Cu, and Zn spinel, hydrogen was produced as the main product at the whole potential, along with other products, such as CO and HCOOH (Figure 5d–f). The FE of Ni spinel to H₂ is higher than 90% at -1.1 V vs. RHE (Figure 5d). Similarly, for the Cu and Zn spinel, the formation of H₂ is still the major product; and the selectivity toward H₂, CO, and HCOOH is less potential-dependent (Figure 5e,f). For Ni and Zn spinel, the FE of H₂ is slightly lower than that of Cu spinel, e.g., 82 and 90% at -0.9 V vs. RHE and the C₁ product FE of less than 20% was also observed (Figures S10 and S11). The comparison of partial current density for H₂, CO, and formate production with different catalysts is shown in Figure 5g–i. It can be seen that the partial current density for H₂ species production would remarkably increase along with the raise of polarization potential, approximate 12.1 mA cm⁻² with Ni spinel, 10.6 mA cm⁻² with Cu spinel and 14.6 mA cm⁻² with Zn spinel at -1.1 V vs. RHE, indicative of H₂ as the main product from the water.

The stability of Ni, Cu, and Zn spinel was evaluated using *i*-*t* measurement at -0.9 V vs. RHE under a continuous flow of CO₂ (Figure 5j–l). Figure 5j,l showed that the Ni and Zn spinel were relatively more stable than Cu spinel and maintained their excellent activity after 6 h at -0.9 V vs. RHE. Meanwhile, for Ni, Zn, and Cu spinel, the FEs of CO and HCOOH are stably maintained throughout the whole CO₂RR process, respectively.

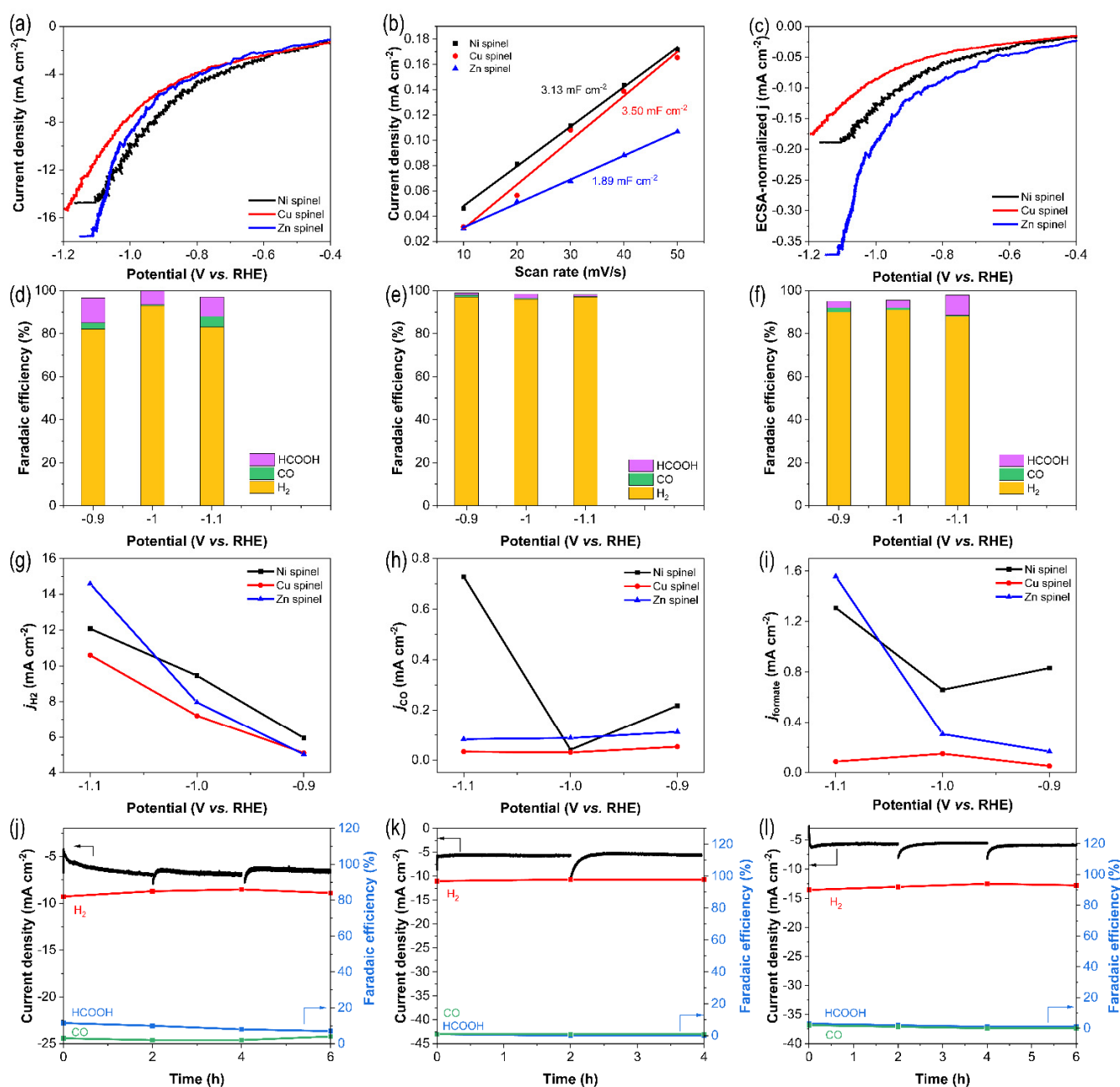


Figure 5. CO₂RR performance of Ni, Cu, and Zn spinel: (a) LSV curves, (b) plots showing the extraction of the C_{dl} for the estimation of the ECSA, (c) ECSA-normalized LSV curves, (d–f) FE of major products vs. potential for the Ni, Cu, and Zn spinel catalyst at a potential range of -0.9 V to -1.1 V in 0.1 M KHCO₃, (g) H₂, (h) CO, and (i) formate current density plots as a function of potential (vs. RHE) during CO₂ flow rate of 20 sccm, (j–l) stability test of Ni, Cu, and Zn spinel, Left y -axis: the current density (j) of Ni, Cu, and Zn spinel at -0.9 V vs. RHE. Right y -axis: the faradaic efficiency of H₂, HCOOH, and CO.

Besides, we also discuss the chemical composition and valence state of Zn, Ni, and Cu spinel coated on carbon paper before and after the CO₂RR. As shown in Figure 6a, the M 2p_{3/2} signals (M = Co, Zn) were negatively shifted by 0.7 and 0.5 eV, compared to those for fresh Zn spinel. The negative shift confirms the electronic charge redistribution on their atomic interface between Zn–Co. In the Ni spectra (Figure 6b), the valence states of Ni²⁺ and Ni³⁺ were relatively stable without significant changes, while the Co³⁺ 2p_{3/2} and Co²⁺ 2p_{3/2} shifted to the lower binding energy after the CO₂RR for Ni spinel, indicating a strong

charge transfer from Co to O atom. For Cu spinel (Figure 6c), the significant binding energy shifted in XPS spectra of Cu and Co also suggests the strong charge transfer from Cu to Co atom through the Cu—Co atomic interface, leading to the decreased electron density of Cu.

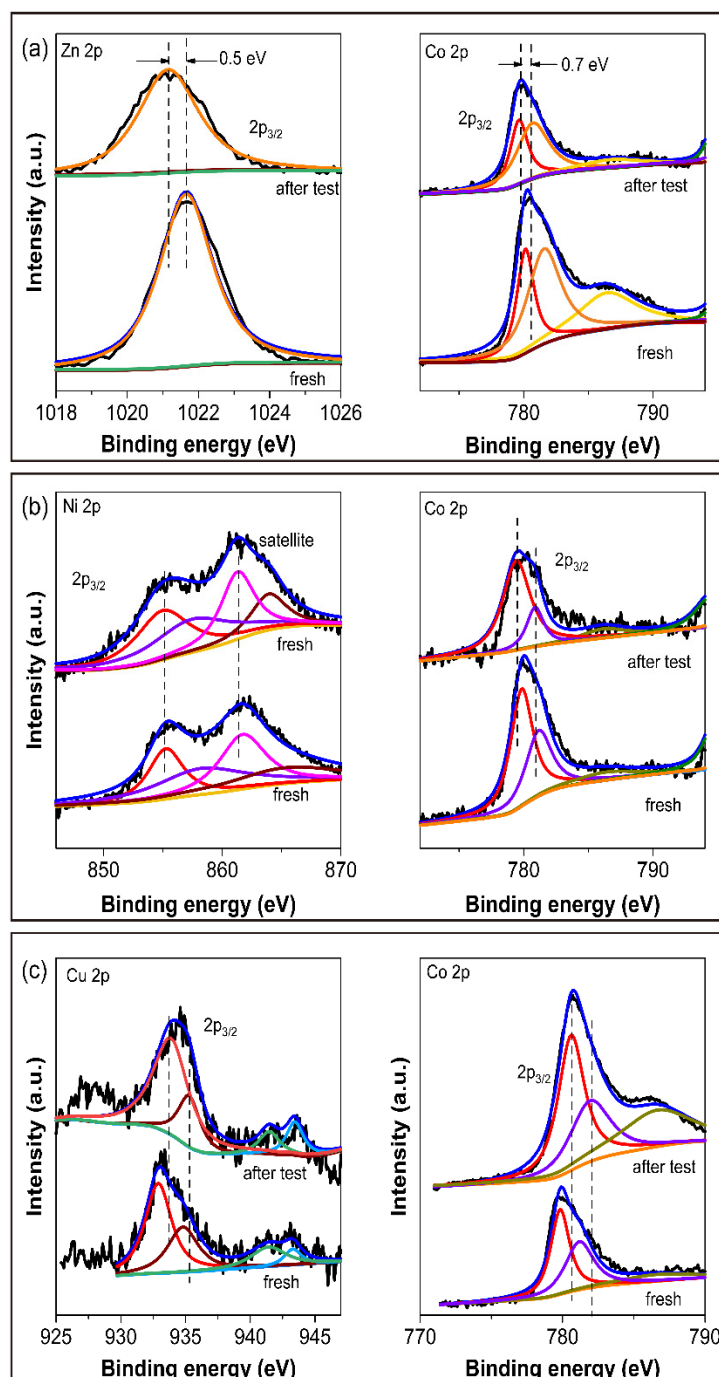


Figure 6. XPS spectra of spinels (cf. both before and after the reaction): (a) Zn and Co 2p spectra of Zn spinel; (b) Ni 2p and Co 2p spectra of Ni spinel; (c) Cu 2p and Co 2p spectra of Cu spinel.

4. Material and Methods

4.1. Materials

Zinc nitrate hexahydrate, cobalt nitrate hexahydrate, copper nitrate trihydrate, and nickel nitrate hexahydrate were purchased from Sigma-Aldrich, Darmstadt, Germany. Pure urea ethanol was obtained from Fisher Scientific, Waltham, MA USA.

4.2. Synthesis of Different Spinel Catalysts

The ZnCo_2O_4 , CuCo_2O_4 , and NiCo_2O_4 spinel catalysts were prepared by a co-precipitation followed by hydrothermal treatment under autogenous pressure. One mmol of $\text{Zn}(\text{NO}_3)_2 \cdot 6\text{H}_2\text{O}$, $\text{Cu}(\text{NO}_3)_2 \cdot 3\text{H}_2\text{O}$, and $\text{Ni}(\text{NO}_3)_2 \cdot 6\text{H}_2\text{O}$ were mixed individually with two mmol of $\text{Co}(\text{NO}_3)_2 \cdot 6\text{H}_2\text{O}$ in 50 mL of deionized water (DI) under vigorous stirring. A total of 60 mmol of urea dissolved in 100 mL of deionized water was then added drop by drop into the above solutions as a precipitating agent at pH 11–12 and thereafter stirred for 30 min. Then, the total contents were poured into a 200 mL Teflon-lined stainless-steel autoclave and subjected to hydrothermal treatment at 180 °C for 6 h. After hydrothermal treatment, the obtained precipitate was filtered and washed with deionized water and ethanol. Finally, the washed cake was dried in an electric oven for 6 h at 60 °C and calcined at 400 °C for 3 h in air at a heating rate of 3 °C/min.

4.3. Characterization of Catalysts

The crystallographic structure of all prepared solid samples was characterized by X-ray diffraction using Bruker diffractometer (Bruker D8 Advance, Karlsruhe, Germany) equipped with copper $\text{K}\alpha$ ($\lambda = 1.5405 \text{ \AA}$) and a monochromator at 40 kV and 40 mA, in the 2θ range of 5–80°. The HRTEM images of the samples were obtained using a FEI Tecnai G2 F30 TEM microscope, in Bright Field (BF) imaging mode. The samples were prepared for TEM image analysis by dispersing catalyst powder in alcohol by ultra-sonication, and a droplet of solution was dropped onto ultra-thin carbon film. The BET surface area, total pore volume, and pore radius of different spinel catalysts were determined from results of N_2 adsorption/desorption experiments performed at -196 °C using a Quantachrome Autosorb-iQ instrument after degassing the samples at 120 °C for 5 h. The surface elemental compositions of the samples were analyzed by X-ray photoelectron spectroscopy utilizing a Thermo Fisher scientific with monochromatic X-rays of Al $\text{K}\alpha$ ~ -10 to 1350 eV radiation at a size of 400 μm at a pressure of 10^{-9} mbar. A full-pass energy spectrum of 200 eV and in a narrow 50 eV band was applied. The binding energy of the transverse carbon line (C 1 s) was used for calibration, and the positions of the peaks were corrected relative to the C 1 s signal position.

4.4. Electrochemical Measurements

Electrochemical CO_2 reduction was performed using CH instruments 760E potentiostat equipped with a three-electrode system at room temperature in CO_2 -saturated 0.1 M KHCO_3 (pH = 6.8). Before conducting the test, CO_2 was continuously fed into the cathode compartment (20 sccm, 30 min) to form CO_2 -saturated 0.1 M KHCO_3 . The Pt electrode was used as a counter electrode and Ag/AgCl electrode as the reference electrode. An H-type device made up of two compartment cells, separated by a Nafion-117 proton-exchange membrane was used to separate the cathode and anode, as well as prevent diffusion of products. Linear sweep voltammetry (LSV) scans were carried out in CO_2 saturated 0.1 M KHCO_3 solution at a scan rate of 50 mV s^{-1} . A total of 5 mg of Zn, Ni, and Cu spinel powder were dispersed into a solution containing 500 μL isopropanol and 500 μL deionized water and 40 μL of Nafion solution (5%); subsequently, the ink was dripped onto carbon paper (5 cm \times 1 cm). The electrolyte solution was saturated with CO_2 before the tests and the potential was converted to RHE according to following equation.

$$E (\text{V vs. RHE}) = E (\text{V vs. Ag/AgCl}) + 0.197 \text{ V} + 0.0591 \times \text{pH}$$

The electrochemical active surface area (ECSA)-normalized current density for as-prepared catalysts was calculated by:

$$\text{ECSA-normalized current density} = \text{current density} \times C_s / C_{dl}$$

where C_s is the specific capacitance. In this work, 0.04 mF cm^{-2} was adopted as the value of C_s based on previously reported electrocatalysts [36,37].

The *i-t* curve was measured at different potentials and the products were analyzed using gas chromatography (GC) and NMR. The quantification of gas products (H₂ and CO) was obtained from the peak areas using the standard calibration curves. The gas samples were analyzed, using ruimin gas chromatographic instrument (GC) equipped with a thermal conductivity detector. The liquid products were analyzed by using proton nuclear magnetic resonance (Bruker Avance 600 MHz spectrometer) with dimethyl sulfoxide (DMSO) as an internal standard. In each of the NMR measurements, 0.6 mL of product solution (30 mL of the electrolyte was mixed with 2 μ L dimethyl sulfoxide (DMSO) as an internal standard) and 0.06 mL deuterated water (D₂O, to lock the magnetic field) was added. The one dimensional ¹H spectrum was measured with water suppression.

5. Conclusions

In this study, nanosized Cu, Ni, and Zn cobaltites were synthesized by a simple hydrothermal method under autogenous pressure and subsequent calcination at 400 °C in air. The results have shown that the synthesis of spinels was successful confirmed by XRD results. The morphology and particle sizes of the spinels were investigated by using HRTEM analysis. The current density of the mesoporous NiCo₂O₄ is significantly higher than that of CuCo₂O₄ and ZnCo₂O₄ spinels over the whole potential range. It is indicative of Cu, and Zn spinel is slightly less active in terms of its overpotential to reduce CO₂. Hydrogen was produced as the main product at the whole potential, along with other products, such as CO and HCOOH. The synthesized Ni and Zn spinel were relatively more stable than the Cu spinel, maintained their excellent activity, and delivered a durable catalyst lifetime. Information related to the structure-reactivity relationship has also been provided based on the available characterization and electrochemical data. The proper understanding of higher selectivity toward hydrogen and/or poorer selectivity of carbon-based products will allow us to develop a future generation of effective spinel-derived catalysts, which could have immense application in the distant future.

Supplementary Materials: The following supporting information can be downloaded at: <https://www.mdpi.com/article/10.3390/catal12080893/s1>, Figure S1: XPS survey spectrum of (a) NiCo₂O₄, (b) CuCo₂O₄, (c) ZnCo₂O₄; Figure S2: Deconvoluted X-ray photoelectron spectra for CuCo₂O₄, NiCo₂O₄ and ZnCo₂O₄ before reaction; Figure S3: Ni spinel was evaluated at different times in CO₂-saturated 0.1 M KHCO₃ and reproduced independently by two different systems; Figure S4: Cu spinel was evaluated at different times in CO₂-saturated 0.1 M KHCO₃ and reproduced independently by two different systems; Figure S5: Zn spinel was evaluated at different times in CO₂-saturated 0.1 M KHCO₃ and reproduced independently by two different systems; Figure S6: Cyclic voltammogram (CV) curves of Ni spinel materials in the non-Faradaic potential region recorded at different scan rates (10–50 mV s⁻¹); Figure S7: Cyclic voltammogram (CV) curves of Cu spinel materials in the non-Faradaic potential region recorded at different scan rates (10–50 mV s⁻¹); Figure S8: Cyclic voltammogram (CV) curves of Zn spinel materials in the non-Faradaic potential region recorded at different scan rates (10–50 mV s⁻¹); Figure S9: Nyquist plots of Ni, Zn and Cu spinel in CO₂-saturated 0.1 M KHCO₃; Figure S10: The FE of H₂ for the different catalysts in the potential range of –0.9 to –1.1 V; Figure S11: The FE of C₁ product for the different catalysts in the potential range of –0.9 to –1.1 V; Table S1: Summary of the electrocatalysts toward the CO₂ reduction reaction. References [30,38–43] are cited in the Supplementary Materials.

Author Contributions: Conceptualization, M.M.M.M. and A.D.C.; methodology, W.B. and L.G.; software, L.G.; validation, K.N., M.A.S. and A.A.; formal analysis, N.H.K.; investigation, S.A.-F.; resources, A.A.; data curation, M.A.S.; writing—original draft preparation, K.N.; writing—review and editing, M.M.M.M. and A.D.C.; visualization, L.G.; supervision, A.D.C.; project administration, M.M.M.M.; funding acquisition, M.M.M.M. All authors have read and agreed to the published version of the manuscript.

Funding: Deputyship for Research & Innovation, Ministry of Education in Saudi Arabia, Project number IFPRC-108-130-2020.

Data Availability Statement: The data presented in this study are available in Supplementary Materials.

Acknowledgments: The authors extend their appreciation to the Deputyship for Research & Innovation, Ministry of Education in Saudi Arabia for funding this research work through project number IFPRC-108-130-2020 and the Deanship of Scientific Research (DSR), King Abdulaziz University, Jeddah, Saudi Arabia. Support from a start-up research grant from Wuhan University (China) and the National Natural Science Foundation of China (NSFC) (Grant No. 22050410276 to A.D.C.) is also acknowledged.

Conflicts of Interest: The authors claim that they do not have any known conflicting financial interests or personal affiliations that may seem to have impacted the work presented in this study.

References

1. Verma, S.; Lu, X.; Ma, S.; Masel, R.I.; Kenis, P.J.A. The Effect of Electrolyte Composition on the Electroreduction of CO₂ to CO on Ag Based Gas Diffusion Electrodes. *Phys. Chem. Chem. Phys.* **2016**, *18*, 7075–7084. [[CrossRef](#)] [[PubMed](#)]
2. Kim, B.; Hillman, F.; Ariyoshi, M.; Fujikawa, S.; Kenis, P.J.A. Effects of Composition of the Micro Porous Layer and the Substrate on Performance in the Electrochemical Reduction of CO₂ to CO. *J. Power Sources* **2016**, *312*, 192–198. [[CrossRef](#)]
3. Xiong, P.; Yang, F.; Ding, Z.; Jia, Y.; Liu, J.; Yan, X.; Chen, X.; Yang, C. Preparation and Electrocatalytic Properties of Spinel CoFe_{3-x}O₄ Nanoparticles. *Int. J. Hydrogen Energy* **2020**, *45*, 13841–13847. [[CrossRef](#)]
4. Khdary, N.H.; Alayyar, A.S.; Alsarhan, L.M.; Alshihri, S.; Mokhtar, M. Metal Oxides as Catalyst/Supporter for CO₂ Capture and Conversion, Review. *Catalysts* **2022**, *12*, 300. [[CrossRef](#)]
5. Glazer, A.M. *Crystallography: A Very Short Introduction*; Oxford University Press: Oxford, UK, 2016; ISBN 9780198717591.
6. Singh, S.K.; Dhavale, V.M.; Kurungot, S. Surface-Tuned Co₃O₄ Nanoparticles Dispersed on Nitrogen-Doped Graphene as an Efficient Cathode Electrocatalyst for Mechanical Rechargeable Zinc-Air Battery Application. *ACS Appl. Mater. Interfaces* **2015**, *7*, 21138–21149. [[CrossRef](#)] [[PubMed](#)]
7. Ramsundar, R.M.; Debgupta, J.; Pillai, V.K.; Joy, P.A. Co₃O₄ Nanorods—Efficient Non-Noble Metal Electrocatalyst for Oxygen Evolution at Neutral pH. *Electrocatalysis* **2015**, *6*, 331–340. [[CrossRef](#)]
8. Jin, H.; Wang, J.; Su, D.; Wei, Z.; Pang, Z.; Wang, Y. In-Situ Cobalt-Cobalt Oxide/N-Doped Carbon Hybrids as Superior Bi-Functional Electrocatalysts for Hydrogen and Oxygen Evolution. *J. Am. Chem. Soc.* **2015**, *137*, 2688–2694. [[CrossRef](#)] [[PubMed](#)]
9. Hamdani, M.; Singh, R.N.; Chartier, P. Co₃O₄ and Co-Based Spinel Oxides Bifunctional Oxygen Electrodes. *Int. J. Electrochem. Sci.* **2010**, *5*, 556–577.
10. Wang, J.; Wang, Q.; She, W.; Xie, C.; Zhang, X.; Sun, M.; Xiao, J.; Wang, S. Tuning the Electron Density Distribution of the Co-N-C Catalysts through Guest Molecules and Heteroatom Doping to Boost Oxygen Reduction Activity. *J. Power Sources* **2019**, *418*, 50–60. [[CrossRef](#)]
11. Raveau, B.; Seikh, M.M. Magnetic and Physical Properties of Cobalt Perovskites. In *Handbook of Magnetic Materials*; Elsevier B.V.: Amsterdam, The Netherlands, 2015; Volume 23, pp. 161–289.
12. Gao, S.; Lin, Y.; Jiao, X.; Sun, Y.; Luo, Q.; Zhang, W.; Li, D.; Yang, J.; Xie, Y. Partially Oxidized Atomic Cobalt Layers for Carbon Dioxide Electroreduction to Liquid Fuel. *Nature* **2016**, *529*, 68–71. [[CrossRef](#)]
13. Harris, V.G. Microwave magnetic materials. In *Handbook of Magnetic Materials*; Elsevier: Amsterdam, The Netherlands, 2012; pp. 1–63.
14. Basahel, S.N.; Abd El-Maksod, I.H.; Abu-Zied, B.M.; Mokhtar, M. Effect of Zr⁴⁺ doping on the stabilization of ZnCo-mixed oxide spinel system and its catalytic activity towards N₂O decomposition. *J. Alloys Compd.* **2010**, *493*, 630–635. [[CrossRef](#)]
15. Bruce, P.G. *Solid State Electrochemistry*; Cambridge University Press: Cambridge, UK, 1995; ISBN 0521400074.
16. Singh, R.-N.; Hamdani, M.; Koenig, J.-F.; Poillerat, G.; Gautier, J.L.; Chartier, P. Thin Films of CO₃O₄ and NiCo₂O₄ Obtained by the Method of Chemical Spray Pyrolysis for Electrocatalysis III. The Electrocatalysis of Oxygen Evolution. *J. Appl. Electrochem.* **1990**, *20*, 442–446. [[CrossRef](#)]
17. Singh, R.N.; Koenig, J.-F.; Poillerat, G.; Chartier, P. Electrochemical Studies on Protective Thin CO₃O₄ and NiCo₂O₄ Films Prepared on Titanium by Spray Pyrolysis for Oxygen Evolution. *J. Electrochem. Soc.* **1990**, *137*, 1408–1413. [[CrossRef](#)]
18. Rashkova, V.; Kitova, S.; Konstantinov, I.; Vitanov, T. Vacuum Evaporated Thin Films of Mixed Cobalt and Nickel Oxides as Electrocatalyst for Oxygen Evolution and Reduction. *Electrochim. Acta* **2002**, *47*, 1555–1560. [[CrossRef](#)]
19. Zhao, Q.; Yan, Z.; Chen, C.; Chen, J. Spinels: Controlled Preparation, Oxygen Reduction/Evolution Reaction Application, and Beyond. *Chem. Rev.* **2017**, *117*, 10121–10211. [[CrossRef](#)] [[PubMed](#)]
20. Shi, R.; Zhang, Y.; Wang, Z. Facile Synthesis of a ZnCo₂O₄ Electrocatalyst with Three-Dimensional Architecture for Methanol Oxidation. *J. Alloys Compd.* **2019**, *810*, 151879. [[CrossRef](#)]
21. Anu Prathap, M.U.; Srivastava, R. Synthesis of NiCo₂O₄ and Its Application in the Electrocatalytic Oxidation of Methanol. *Nano Energy* **2013**, *2*, 1046–1053. [[CrossRef](#)]
22. Silambarasan, M.; Padmanathan, N.; Ramesh, P.S.; Geetha, D. Spinel CuCo₂O₄ Nanoparticles: Facile One-Step Synthesis, Optical, and Electrochemical Properties. *Mater. Res. Express* **2016**, *3*, 095021. [[CrossRef](#)]
23. Hao, S.; Zhang, B.; Ball, S.; Copley, M.; Xu, Z.; Srinivasan, M.; Zhou, K.; Mhaisalkar, S.; Huang, Y. Synthesis of Multimodal Porous ZnCo₂O₄ and Its Electrochemical Properties as an Anode Material for Lithium Ion Batteries. *J. Power Sources* **2015**, *294*, 112–119. [[CrossRef](#)]

24. Li, X.; Jiang, L.; Zhou, C.; Liu, J.; Zeng, H. Integrating Large Specific Surface Area and High Conductivity in Hydrogenated NiCo₂O₄ Double-Shell Hollow Spheres to Improve Supercapacitors. *NPG Asia Mater.* **2015**, *7*, e165. [[CrossRef](#)]
25. Lu, L.; Min, F.; Luo, Z.; Wang, S.; Teng, F.; Li, G.; Feng, C. Synthesis and Electrochemical Properties of CuCo₂O₄ as Anode Material for Lithium-Ion Battery. *J. Nanosci. Nanotechnol.* **2017**, *17*, 4763–4771. [[CrossRef](#)]
26. Xiao, X.; Wang, G.; Zhang, M.; Wang, Z.; Zhao, R.; Wang, Y. Electrochemical Performance of Mesoporous ZnCo₂O₄ Nanosheets as an Electrode Material for Supercapacitor. *Ionics* **2018**, *24*, 2435–2443. [[CrossRef](#)]
27. Wu, H.; Qin, M.; Zhang, L. NiCo₂O₄ Constructed by Different Dimensions of Building Blocks with Superior Electromagnetic Wave Absorption Performance. *Compos. Part B Eng.* **2020**, *182*, 107620. [[CrossRef](#)]
28. Vijayakumar, S.; Lee, S.H.; Ryu, K.S. Hierarchical CuCo₂O₄ Nanobelts as a Supercapacitor Electrode with High Areal and Specific Capacitance. *Electrochim. Acta* **2015**, *182*, 979–986. [[CrossRef](#)]
29. Zhu, J.; Gao, Q. Mesoporous MCo₂O₄ (M = Cu, Mn and Ni) Spinel: Structural Replication, Characterization and Catalytic Application in CO Oxidation. *Microporous Mesoporous Mater.* **2009**, *124*, 144–152. [[CrossRef](#)]
30. Sekar, P.; Calvillo, L.; Tubaro, C.; Baron, M.; Pokle, A.; Carraro, F.; Martucci, A.; Agnoli, S. Cobalt Spinel Nanocubes on N-Doped Graphene: A Synergistic Hybrid Electrocatalyst for the Highly Selective Reduction of Carbon Dioxide to Formic Acid. *ACS Catal.* **2017**, *7*, 7695–7703. [[CrossRef](#)]
31. Parveen, S.; Nguyen, H.H.; Premkumar, T.; Puschmann, H.; Govindarajan, S. Nano Spinel Cobaltites and Their Catalytic and Electrochemical Properties: Facile Synthesis of Metal (Co, Ni, and Zn) and Mixed Metal (Co–Ni and Co–Zn) Complexes of Schiff Bases Prepared from α -Ketoglutaric Acid and Ethyl Carbazate. *New J. Chem.* **2020**, *44*, 12729–12740. [[CrossRef](#)]
32. Lu, X.F.; Wu, D.J.; Li, R.Z.; Li, Q.; Ye, S.H.; Tong, Y.X.; Li, G.R. Hierarchical NiCo₂O₄ Nanosheets@hollow Microrod Arrays for High-Performance Asymmetric Supercapacitors. *J. Mater. Chem. A* **2014**, *2*, 4706–4713. [[CrossRef](#)]
33. Moulder, J.F.; Stickle, W.F.; Sobol, P.E.; Bomben, K.D.; Chastain, J. *Handbook of X-ray Photoelectron Spectroscopy A Reference Book of Standard Spectra for Identification and Interpretation of XPS Data*; Perkin-Elmer: Waltham, MA, USA, 1979.
34. Hu, L.; Qu, B.; Li, C.; Chen, Y.; Mei, L.; Lei, D.; Chen, L.; Li, Q.; Wang, T. Facile Synthesis of Uniform Mesoporous ZnCo₂O₄ Microspheres as a High-Performance Anode Material for Li-Ion Batteries. *J. Mater. Chem. A* **2013**, *1*, 5596–5602. [[CrossRef](#)]
35. Fang, Y.Y.; Wang, X.Z.; Chen, Y.Q.; Dai, L.Y. NiCo₂O₄ Nanoparticles: An Efficient and Magnetic Catalyst for Knoevenagel Condensation. *J. Zhejiang Univ. Sci. A* **2020**, *21*, 74–84. [[CrossRef](#)]
36. Zheng, W.; Liu, M.; Lee, L.Y.S. Best Practices in Using Foam-Type Electrodes for Electrocatalytic Performance Benchmark. *ACS Energy Lett.* **2020**, *5*, 3260–3264. [[CrossRef](#)]
37. Huang, Y.; Jiang, L.W.; Shi, B.Y.; Ryan, K.M.; Wang, J.J. Highly Efficient Oxygen Evolution Reaction Enabled by Phosphorus Doping of the Fe Electronic Structure in Iron–Nickel Selenide Nanosheets. *Adv. Sci.* **2021**, *8*, 2101775. [[CrossRef](#)] [[PubMed](#)]
38. Zhang, Q.; He, A.; Dong, W.; Du, J.; Liu, Z.; Tao, C. Co, N Co-Doped Porous Carbon Supported Spinel Co₃O₄ for Highly Selective Electroreduction of CO₂ to Formate. *Vacuum* **2022**, *197*, 110803. [[CrossRef](#)]
39. Gao, S.; Jiao, X.; Sun, Z.; Zhang, W.; Sun, Y.; Wang, C.; Hu, Q.; Zu, X.; Yang, F.; Yang, S.; et al. Ultrathin Co₃O₄ Layers Realizing Optimized CO₂ Electroreduction to Formate. *Angew. Chem.* **2016**, *128*, 708–712. [[CrossRef](#)]
40. Yang, Y.; He, A.; Yang, M.; Zou, Q.; Li, H.; Liu, Z.; Du, J. Selective electroreduction of CO₂ to ethanol over a highly stable catalyst derived from polyaniline/CuBi₂O₄. *Catal. Sci. Technol.* **2021**, *11*, 5908–5916. [[CrossRef](#)]
41. Karim, K.M.R.; Tarek, M.; Sarkar, S.M.; Mouras, R.; Ong, H.R.; Abdullah, H.; Cheng, C.K.; Khan, M.M.R. Photoelectrocatalytic Reduction of CO₂ to Methanol over CuFe₂O₄@PANI Photocathode. *Int. J. Hydrogen Energy* **2021**, *46*, 24709–24720. [[CrossRef](#)]
42. Tarek, M.; Rezaul Karim, K.M.; Sarkar, S.M.; Deb, A.; Ong, H.R.; Abdullah, H.; Cheng, C.K.; Rahman Khan, M.M. Hetero-Structure CdS–CuFe₂O₄ as an Efficient Visible Light Active Photocatalyst for Photoelectrochemical Reduction of CO₂ to Methanol. *Int. J. Hydrogen Energy* **2019**, *44*, 26271–26284. [[CrossRef](#)]
43. Simon, C.; Zander, J.; Kottakkat, T.; Weiss, M.; Timm, J.; Roth, C.; Marschall, R. Fast Microwave Synthesis of Phase-Pure Ni₂FeS₄ Thiospinel Nanosheets for Application in Electrochemical CO₂ Reduction. *ACS Appl. Energy Mater.* **2021**, *4*, 8702–8708. [[CrossRef](#)]